Infrared photocarrier radiometry of semiconductors: Physical principles, quantitative depth profilometry, and scanning imaging of deep subsurface electronic defects

Andreas Mandelis, Jerias Batista,* and Derrick Shaughnessy
Center for Advanced Diffusion-Wave Technologies, Department of Mechanical and Industrial Engineering, University of Toronto, Toronto, Canada M5S 3G8

(Received 31 January 2003; published 21 May 2003)

Laser-induced infrared photocarrier radiometry (PCR) is introduced theoretically and experimentally through deep subsurface scanning imaging and signal frequency dependencies from Si wafers. A room-temperature InGaAs detector (0.8–1.8 μm) with integrated amplification electronics is used instead of the liquid-nitrogen-cooled HgCdTe photodetector (2–12 μm) of conventional photothermal radiometry. PCR measures purely electronic carrier-wave (CW) recombination. The InGaAs detector completely obliterates the thermal-infrared emission band (8–12 μm), unlike the known photothermal signal types, which invariably contain combinations of carrier-wave and thermal-wave infrared emissions due to the concurrent lattice absorption of the incident beam and nonradiative heating. The PCR theory is presented as infrared depth integrals of CW density profiles. Experimental aspects of this methodology are given, including the determination of photocarrier transport parameters through modulation frequency scans, as well as CW scanning imaging. The PCR coordinate scans at the front surface of 500$-\mu$m-thick Si wafers with slight back-surface mechanical defects can easily ''see'' and create clear images of the defects at modulation frequencies up to 100 kHz, at laser-beam optical penetration depth $\sim$1 μm below the surface (at 514 nm). The physics of the contrast mechanism for the nonthermal nature of the PCR signal is described: it involves self-reabsorption of CW-recombination-generated IR photons emitted by the photoexcited carrier-wave distribution depth profile throughout the wafer bulk. The distribution is modified by enhanced recombination at localized or extended defects, even as remote as the back surface of the material. The high-frequency, deep-defect PCR images thus obtained prove that very-near-surface (where optoelectronic device fabrication takes place) photocarrier generation can be detrimentally affected not only by local electronic defects as is commonly assumed, but also by defects in remote wafer regions much deeper than the extent of the electronically active thin surface layer.

DOI: 10.1103/PhysRevB.67.205208 PACS number(s): 78.20.Ci, 72.20.Jv, 07.60.Dq, 78.30.Am

I. INTRODUCTION

In recent years the development of laser-induced infrared photothermal radiometry (PTR) of semiconductors in our laboratory[1–9] and elsewhere[10] as a quantitative methodology for the measurement of transport properties of semiconductors has led to several advances in the noncontact measurement of four transport parameters: bulk recombination lifetime, (two) surface recombination velocities, and carrier diffusion coefficient in Si (Refs. 1–10) and GaAs (Ref. 11). Reviews of the subject matter have been presented by Mandelis[12] and Christofides *et al.*[13]. The major advantage of PTR over other photothermal techniques, such as photomodulated thermoreflectance (PMOR), has been found to be the higher sensitivity of PTR to the photoexcited free-carrier-density-wave (the modulated-laser driven oscillating electronic diffusion wave[14]) than PMOR.[15,16] This advantage exists due to domination of the free-carrier wave over the superposed thermal-wave (TW) contributions to the PTR signal. Even so, the ever-present thermal-wave contributions due to direct lattice absorption, followed by nonradiative energy conversion and blackbody (thermal-infrared) emissions, have resulted in the PTR signal interpretational and computational difficulties due to the large number of variables involved.[5] Therefore, confidence in the measured values of the four electronic transport properties is always accompanied by the hurdle of assuring uniqueness of the measured set of parameters in any given situation. With our development of the PTR methodology as a quantitative technique for nondestructive semiconductor diagnostics, we found[4,5] that early measurements reported without regard to computational uniqueness[17] using simplified theoretical fits to frequency-scan signals cannot be unique and therefore reliable.

Several schemes to enhance the photoexcited free-carrier-density-wave (or simply ''carrier-wave,'' CW) contributions to the photothermal signal have been proposed, such as working in the high-frequency, CW dominated, regime with PTR[12], or using a tightly focused pump laser beam in PMOR.[18] However, the presence of even a diminished TW component in the high-frequency PTR will be shown in this work to have significant effects on the measured values of the transport parameters, to compromise sensitivity to the carrier wave and to complicate the task of physical interpretation of the signal, thus raising the question of uniqueness of the measured set of solid-state transport parameters. On the other hand, very tight focusing of the pump laser beam in PMOR tends to give rise to usually undesirable nonlinear thermal and electronic effects,[15,19,20] besides being unable to sufficiently eliminate the TW component of the signal.[21] Therefore, given the fundamental and practical importance of developing an all-optical, nondestructive and nonintrusive diagnostic methodology for monitoring *only* the transport properties of semiconductors, we concluded that the search for a purely carrier-wave laser-based detection methodology

 ©2003 The American Physical Society

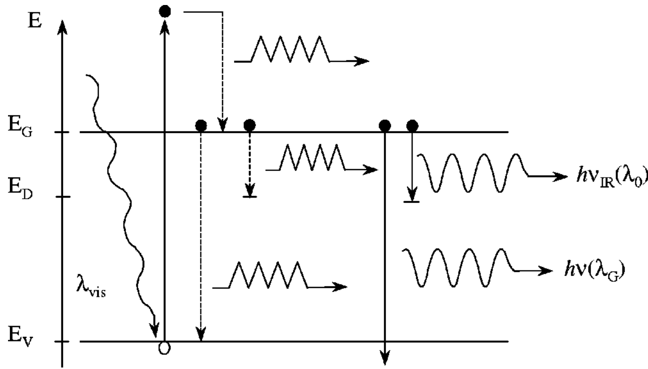

FIG. 1. *n*-type semiconductor energy-band diagram showing excitation and recombination processes. Energy emission processes include nonradiative intraband and interband decay accompanied by phonon emission, as well as direct band-to-band recombination radiative emissions of energy $\hbar\omega(\lambda_G)$ and band-to-defect/impurity-state recombination IR emissions of energy $\hbar\omega_{IR}(\lambda_D)$.

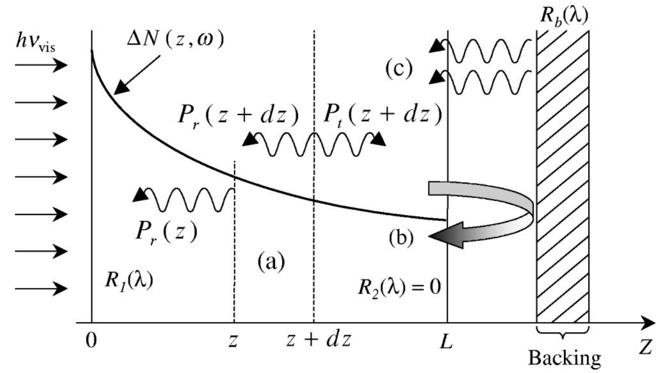

FIG. 2. Cross-sectional view of contributions to front-surface radiative emissions of IR photons from (a) a semiconductor strip of thickness dz at depth z; (b) reentrant photons from the back surface due to reflection from a backing support material; (c) emissive IR photons from the backing at thermodynamic temperature T_b. The carrier-wave depth profile $\Delta N(z,\omega)$ results in a depth dependent IR absorption/emission coefficient due to free-carrier absorption of the infrared photon fields, both ac and dc.

must move in the direction of isolating and eliminating the superposition of thermal-wave contributions to the infrared emission spectrum. In view of the inability of photothermal semiconductor diagnostic methods[13,18] to eliminate the thermal-wave contributions, the development of infrared laser radiometry of semiconductors to optimize this task has been very promising, given the intrinsically higher sensitivity of its photothermal embodiment, PTR, to the photoexcited carrier-density wave than other photothermal techniques, notably PMOR.[16] In this paper, the theory and experimental configuration of infrared laser photocarrier radiometry (PCR), a technique only sensitive to the recombination of free photoexcited carrier-density waves, are introduced. Next, a first application of PCR to depth-profilometric imaging of deep-lying mechanically induced electronic defects in *p*-type Si wafers is presented, along with a comparison of PCR to conventional PTR with regard to quantitative measurements of CW transport properties.

II. THEORY OF INFRARED PHOTOCARRIER RADIOMETRY OF SEMICONDUCTORS

A. Kirchhoff's law and the oscillating carrier wave

In a photoexcited semiconductor of band-gap energy E_G, an externally incident optical source such as a laser beam with super-band-gap energy photons $\hbar\omega_{vis}\geqslant E_G$ will be absorbed and can generate free carriers which may subsequently follow several deexcitation pathways as shown in Fig. 1 for an *n*-type material. Ultrafast decay to the respective band edge (e.g., conduction band) through nonradiative transitions and emission of phonons, will raise the temperature of the semiconductor locally. The free carriers will further diffuse within their statistical lifetime and will recombine with carriers of the opposite sign across the band gap or into impurity and/or defect states within the band gap. The electron-hole recombination mechanism with or without phonon assistance will lead either to nonradiative energy conversion through phonon emissions (e.g., in indirect-gap semiconductors such as Si) which will further raise the temperature, or to radiative decay which will produce photons of near- or sub-band-gap energy. A table of radiative recombination lifetimes at 300 K in Si and other semiconductors has been compiled by Hall.[22] In the presence of impurity or defect states within the band gap, free-carrier decay to one or more of those states may also occur through nonradiative or radiative transitions symbolized by dashed and full arrows, respectively, in Fig. 1. Again, the former will raise the temperature of the semiconductor crystal through phonon coupling to the lattice, whereas the latter will produce photons of energy $E_G-E_D\simeq\hbar\omega_{IR}$. In actual semiconductor materials, there may be a distribution of impurity and defect states into which deexcitation may occur. Therefore, it is more relevant to consider the full spectral range of IR emissions from a photoexcited semiconductor crystal: $\hbar\omega_{IR}=\hbar\omega(\lambda_D)$. If the exciting super-band-gap radiation is intensity modulated at frequency $f=\omega/2\pi$, then the photogenerated free-carrier density constitutes a spatially damped carrier-density wave (CW) (or carrier-diffusion wave,[14]) which oscillates diffusively away from the generating source under its concentration gradient and recombines with a phase lag dependency on a delay time equal to its statistical lifetime τ a structure- and process-sensitive property.[23] Figure 2 shows a virtual cross section of a semiconductor Si wafer where an infrared emission photon distribution is produced following laser radiation absorption and carrier-wave generation. For one-dimensional geometries, such as those obtained with thin crystals and/or use of laser beams of large spot size, only forward- and backward-emitted photons of wavelength λ are depicted. The IR power generated at λ within a spectral bandwidth $d\lambda$ is given by

$$dP_j(z,t;\lambda)=\{W_{NR}[T_T(z,t);\lambda]+\eta_R W_{eR}(\lambda)\}_j d\lambda;\quad j=r,t\quad [\mathrm{W}], \tag{1}$$

where $W_{NR}[T_T(z,t);\lambda]$ is the thermal-infrared power per unit wavelength generated due to temperature rise following

optical absorption, as well as due to other nonradiative decays. The subscripts (r,t) indicate back-propagating ("reflected") or forward-propagating ("transmitted") photon power. $W_{eR}(\lambda)$ is the spectral power per unit wavelength, the product of the recombination transition rate from band to band, or from band edge to defect or impurity state, as the case may be, multiplied by the energy difference between initial and final states. η_R is the quantum yield for IR radiative emission upon carrier recombination into one of these states. $T_T(z,t;\lambda)$ is the total temperature, including background temperature, temperature increase due to thermal-wave oscillation following laser-modulated absorption and optical heating, as well as other nonradiative energy conversion pathways. Therefore,

$$W_{NR}[T_T(z,t);\lambda]=W_P[T_s(z,t);\lambda]+(1-\eta_R)W_{eR}(\lambda)+W_{eH}(\lambda) \quad [\mathrm{W}/\mu\mathrm{m}]. \tag{2}$$

Here, $W_P[T_s(z,t);\lambda]d\lambda$ is the familiar Planck distribution function, or spectral emissive power, representing the rate of radiative recombination within $d\lambda$, and sample volume $\Delta V = A[\alpha_{IR}(\lambda)]^{-1}$ of emitting cross-sectional area A normal to the z axis in Fig. 2, and depth equal to the optical absorption depth at infrared wavelength λ. $\alpha_{IR}(\lambda)$ is the IR absorption coefficient at λ and

$$W_P[T_s(z,t);\lambda]d\lambda=\frac{8\pi h(c_0/n)^2A\,d\lambda}{\lambda^5\{\exp[hc_0/\lambda n k_B T_s(z,t)]-1\}} \quad [\mathrm{W}], \tag{3}$$

(c_0/n) is the speed of light in the medium of refractive index n. $T_s(z,t)$ is made up of only two contributions: background temperature and harmonic optical heating of the lattice at modulation frequency f. The remaining symbols in Eq. (2) have the following meanings: $W_{eH}(\lambda)$ is the thermal IR photon generation power per unit wavelength due to intraband nonradiative deexcitation of hot carriers with energy $\hbar\omega_{vis}-E_G$, Fig. 1. $(1-\eta_R)$ is the nonradiative quantum yield for recombination processes, which generate total power $W_{eR}(\lambda)$ per unit wavelength.

The use of Eq. (3) in describing the thermal emissive power assumes the existence of thermal equilibrium in the semiconductor, a condition known as the principle of detailed balance. It states that the rate of radiative recombination at thermal equilibrium within an emission frequency interval $d\nu$, centered at frequency ν, is equal to the corresponding generation rate of electron-hole pairs by the thermal radiation field present within the semiconductor.[23] Detailed balance is, in itself, a statement of Kirchhoff's theorem,[24] according to which "*for any body in (radiative) thermal equilibrium with its environment, the ratio between the spectral emissive power* $W(T,\lambda)d\lambda$ *and the spectral absorptivity* $a(T,\lambda)$, *for a given photon frequency* $\nu=c/\lambda$ *and temperature T, is equal to the spectral emissive power* $W_P(T,\lambda)d\lambda$, *Eq. (3), of the blackbody for the same frequency and temperature*." Introducing the definition of spectral emissivity

$$e(T,\lambda)\equiv W(T,\lambda)/W_P(T,\lambda), \tag{4}$$

the well-known Kirchhoff law

$$e(T,\lambda)=a(T,\lambda) \tag{5}$$

is obtained. Considering the absorption coefficient $\alpha_{IR}(\lambda,T)$ and the emission coefficient $\epsilon(\lambda,T)$, the radiation density of the blackbody in the medium is given by $\rho(\lambda,T)=\alpha_{IR}(\lambda,T)F_P(\lambda,T)$ $[\mathrm{Jm}^{-3}]$, where $F_P(\lambda,T) = W_P(T,\lambda)/A\tau$ is the blackbody energy flux across the elementary area A within τ, the characteristic emission time. According to Kirchhoff's law, using Eqs. (4) and (5), we find

$$\epsilon(\lambda,T)=\alpha_{IR}(\lambda,T). \tag{6}$$

When an external energy source, such as a laser beam, upsets the charge-carrier-wave distribution equilibrium as is the case with PCR, one needs to proceed with great caution in applying Eq. (6). Clearly, once a super-band-gap photon flux raises free carriers above the equilibrium density in the semiconductor, their recombination rate increases above the equilibrium value, which in turn generates sub-band-gap spectral emissive power $\eta_R W_{eR}(\lambda)d\lambda$. The physical picture involves the emission rate of the thus created IR photons and its comparison to the absorption rate of the same IR photon field by the semiconductor in inducing the reverse optical transitions, since detailed balance requires that the recombination IR radiation should have the same spectrum as the absorbed IR photons of the ambient radiation field.[25] Away from carrier-density equilibrium, the approach of Weinstein[26] may be adopted. Through thermodynamic arguments Weinstein[26] and Bauer[27] conclude that the emission coefficient, defined for spontaneous processes only, is entirely determined by the energy state configuration of the material and by the spontaneous transition probabilities connecting them. Therefore, $\epsilon(\lambda,T)$ is independent of the ambient radiation field. It follows that, for Kirchhoff's law to be valid, it suffices that the quantum states of the medium obey the equilibrium distribution, regardless of the temperature distribution of the radiation field. In low-power laser interactions with electronic carriers, it is easy to justify the Weinstein-Bauer conditions, as long as (i) there exist no intense electromagnetic optical or thermal gradient fields in the semiconductor to upset the quantum configuration of the energy states, driving the structure away from electronic energy equilibrium; (ii) upward electronic transitions following optical absorption result in efficient radiative deexcitations with minimal temperature increase of the lattice; or (iii) even if significant temperature changes occur due to nonradiative decays which may affect the background temperature of the lattice as in the case of CW generation, however, the temperature oscillation itself amounts to only minimal thermal-wave perturbations with no significant consequence in the structure of the energetic manifold of the semiconductor. Under these conditions, the semiconductor can be considered to be at electronic and thermal equilibrium during the oscillation cycle of the photoexcited CW: electronic transitions occur essentially adiabatically, with minimum thermal energy exchange interactions across well-defined electronic state densities. It also follows that the higher the oscillation frequency, the greater the adiabatic character of the transition, leading to a stricter

validation of Kirchhoff's law through complete thermal decoupling of the CW oscillator ensemble, as experimentally observed by use of PTR.[4] Therefore, despite the large ambient radiation field oscillations, Eq. (6) is expected to remain essentially valid away from free-carrier-density equilibrium in PCR. The absence of cross coupling in the emitted power of Eq. (1) is a statement of the adiabatic superposition of thermal-infrared (Planck-mediated) emissions through the $W_{NR}[T_T(z,t);\lambda]$ term, and direct electronic infrared emissions through the $\eta_R W_{eR}(\lambda)$ term under equilibrium (i.e., constant) baseline temperature and a stationary material energy state manifold characterized by a well-defined Fermi level. A by-product of adiabaticity is that the IR spectra of thermal and recombination emissions are independent of each other, a feature that is central to the realization of PCR.

B. Emissive IR power generation in semiconductors

Figure 2 shows an elementary slice of thickness dz centered at depth z in a semiconductor slab. The crystal is supported by a backing, but is not necessarily in contact with the backing. A modulated laser beam at angular frequency $\omega = 2\pi f$ and wavelength λ_{vis} impinges on the front surface of the semiconductor. The super-band-gap radiation is absorbed within a (short) distance from the surface, typically, a few μm, given by $[\alpha(\lambda_{vis})]^{-1}$, where $\alpha(\lambda_{vis})$ is the visible-range absorption coefficient of the pump radiation. The ensuing deexcitation processes generally involve radiative and nonradiative energy release components, resulting in the generation of an IR photon field in the semiconductor involving a relatively broad spectral bandwidth. At thermal and electronic equilibrium, assuming a one-dimensional geometry as a result of a large laser-beam spotsize and/or thin sample, the emitted IR photons have equal probability of being directed toward the front or the back surface of the material. Consider only those photons of wavelength λ generated through recombination and radiative emission which are crossing $z + dz$, traversing the thickness element dz and heading toward the surface $z=0$. The IR power increment $P_r(z,\omega;\lambda) < P_r(z+dz,\omega;\lambda)$ due to self-absorption by the diffusing free-carrier wave, leading to further carrier generation. Therefore, the net absorbed power within the strip dz is given by

$$dP_r(z,\omega;\lambda) \equiv P_r(z+dz,\omega;\lambda) - P_r(z,\omega;\lambda) = \left(\frac{dP_r}{dz}\right) dz = \alpha_{IR}(z,\lambda) P_r(z,\omega;\lambda) dz. \tag{7}$$

To obtain the IR power increment arriving at the surface from the semiconductor interior strip dz, we integrate the right-hand side of this equation from depth z up to the surface $z=0$ and take the spatial dependence of the IR absorption coefficient into account: From Kirchhoff's law, Eq. (6), $\epsilon(\lambda,T)$ can be substituted for $\alpha_{IR}(\lambda,T)$. $\epsilon(\lambda,T)$ is depth dependent because the emission rate depends on the spatial density of the recombining CW. The result of converting Eq. (1) into its frequency domain transform (Fourier component) and then integrating, is

$$dP_r(z,\omega;\lambda) = \{W_{NR}[T_T(z,\omega);\lambda] + \eta_R W_{eR}(\lambda)\} \epsilon(z,\lambda) \times \exp\left[-\int_0^z \epsilon(z',\lambda) dz'\right] dz, \tag{8}$$

where, besides its defining Eq. (7), $dP_r(z,\omega;\lambda)$ also represents, through Kirchhoff's law, the contribution to the total IR emission at the front surface from the emissive source layer dz at subsurface depth z. Allowing for infinite inter-reflections of the back-propagating photons that generate $dP_r(z,\omega;\lambda)$ in Eq. (8) at both surfaces $z=0,L$, with reflectivities $R_1(\lambda)$ and $R_2(\lambda)$, respectively, and summing up all the contributions yields

$$dP_{r1}(z,\omega;\lambda) = \frac{[1-R_1(\lambda)] dP_r(z,\omega;\lambda)}{1 - R_1(\lambda) R_2(\lambda) \exp\left[-2\int_0^L \epsilon(z',\lambda) dz'\right]}, \tag{9}$$

for the IR power transmitted out of the semiconductor through the front surface (reflection); and

$$dP_{t1}(z,\omega;\lambda) = \frac{[1-R_2(\lambda)] R_1(\lambda) dP_r(z,\omega;\lambda) \exp\left[-\int_0^L \epsilon(z',\lambda) dz'\right]}{1 - R_1(\lambda) R_2(\lambda) \exp\left[-2\int_0^L \epsilon(z',\lambda) dz\right]}, \tag{10}$$

for the IR power transmitted out of the semiconductor through the back surface $z=L$ (transmission). Similarly, the photons from the emissive source at depth z, which are directed toward the back surface, after infinite inter-reflections at the interior interfaces of the semiconductor, yield the IR power transmitted out of the semiconductor through the front surface (reflection):

$$dP_{r2}(z,\omega;\lambda) = \frac{[1-R_1(\lambda)] R_2(\lambda) dP_t(z,\omega;\lambda) \exp\left[-\int_0^L \epsilon(z',\lambda) dz'\right]}{1 - R_1(\lambda) R_2(\lambda) \exp\left[-2\int_0^L \epsilon(z',\lambda) dz'\right]}, \tag{11}$$

and for the IR power transmitted through the back surface (transmission):

$$dP_{t2}(z,\omega;\lambda)=\frac{[1-R_2(\lambda)]dP_t(z,\omega;\lambda)}{1-R_1(\lambda)R_2(\lambda)\exp\left[-2\int_0^L \epsilon(z',\lambda)dz\right]},\quad(12)$$

where

$$dP_t(z,\omega;\lambda)=\{W_{NR}[T_T(z,\omega);\lambda]+\eta_R W_{eR}(\lambda)\}\epsilon(z,\lambda)\times\exp\left[-\int_z^L \epsilon(z',\lambda)dz'\right]dz.\quad(13)$$

Adding the two contributions to the power transmitted through $z=0$ and $z=L$, respectively, the following expressions are obtained:

$$dP_r(z,\omega;\lambda)=\frac{[1-R_1(\lambda)]\{W_{NR}[T_T(z,\omega);\lambda]+\eta_R W_{eR}(\lambda)\}\epsilon(z,\lambda)}{1-R_1(\lambda)R_2(\lambda)\exp\left[-2\int_0^L \epsilon(z',\lambda)dz'\right]}\left[\exp\left\{-\int_0^z \epsilon(z',\lambda)dz'\right\}+R_2(\lambda)\exp\left\{-\int_0^{2L-z}\epsilon(z',\lambda)dz'\right\}\right]dz\quad(14)$$

and

$$dP_t(z,\omega;\lambda)=\frac{[1-R_2(\lambda)]\{W_{NR}[T_T(z,\omega);\lambda]+\eta_R W_{eR}(\lambda)\}\epsilon(z,\lambda)}{1-R_1(\lambda)R_2(\lambda)\exp\left[-2\int_0^L \epsilon(z',\lambda)dz'\right]}\left[\exp\left\{-\int_z^L \epsilon(z',\lambda)dz'\right\}+R_1(\lambda)\exp\left\{-\int_{-z}^{L}\epsilon(z',\lambda)dz'\right\}\right]dz.\quad(15)$$

It is evident that the second term inside the bracket of Eq. (14) originates at an image source at $z_0=2L-z$ with respect to the interface at $z=L$ and the second term inside the bracket of Eq. (15) is the image source at $z_0=-z$ with respect to the interface at $z=0$. Equations (14) and (15) can now be used to calculate the total IR power exiting both surfaces of the semiconductor by integration as follows:

$$P_{Tr,t}(\omega)=\int_{\lambda_1}^{\lambda_2}d\lambda\int_0^L dP_{r,t}(z,\omega;\lambda),\quad(16)$$

where $[\lambda_1,\lambda_2]$ is the spectral bandwidth of the IR detector and the integration increment dz is implied in the expression for $dP_{r,t}(z,\omega;\lambda)$. The resulting expression is the IR emissive power of the photoexcited semiconductor in terms of the spectral emission coefficient $\epsilon(\lambda,z)$. In its simplest reduction with $\epsilon(\lambda,z)=\alpha_{IR}(\lambda,z)$, $R_1(\lambda)=R_2(\lambda)\equiv R(\lambda)$, and with only thermal- (Planck-mediated) infrared emission contributions, the spatial integration of Eq. (16) can be easily performed and the resulting formula inserted in Eq. (5) without the wavelength integration to yield the back-propagation spectral emissivity or absorptivity

$$e(T,\lambda)=a(T,\lambda)=\frac{[1-R(\lambda)]\left[1-\exp\left\{-\int_0^L \alpha_{IR}(\lambda,T,z)dz\right\}\right]}{1-R(\lambda)\exp\left\{-2\int_0^L \alpha_{IR}(\lambda,T,z)dz\right\}}.\quad(17)$$

This expression was presented by Chen *et al.*,[28] as a generalization of the well-known expression for a constant IR absorption coefficient.[29,30]

C. Infrared signals from Si wafers and backing support effects

The expressions for the IR spectral emissive power, Eqs. (9)–(15) can be simplified considerably in the case of semiconductor crystals, such as industrial Si wafers, with polished front surface and nonpolished, matte, back surface which scatters the IR radiation with minimal or no reflected power. On setting $R_2(\lambda)\approx 0$ and allowing for a backing support material of reflectivity $R_b(\lambda)$ in contact with, or at some distance d away from, the semiconducting sample back surface, the fraction of the radiation generated at depth z within dz, which leaves the back surface and is reflected back into

the sample is $dP_b(z=L,\omega;\lambda)=R_b(\lambda)dP_t(z,\omega;\lambda)$ from Eq. (15). This acts as an additional source, which contributes to the IR power from the strip dz at the front surface

$$dP_b(z,\omega;\lambda)\approx[1-R_1(\lambda)]R_b(\lambda)\{W_{NR}[T_T(z,\omega);\lambda]+\eta_R W_{eR}(\lambda)\}\epsilon(z,\lambda)\left[\exp\left\{-\int_z^L \epsilon(z',\lambda)dz'\right\}+R_1(\lambda)\exp\left\{-\int_{-z}^L \epsilon(z',\lambda)dz'\right\}\right]\times\exp\left[-\int_0^L \epsilon(z',\lambda)dz'\right]dz. \tag{18}$$

Therefore, instead of Eq. (14), the spectral emissive power at $z=0$ from depth z becomes approximately

$$dP_r(z,\omega;\lambda)\approx[1-R_1(\lambda)]\{W_{NR}[T_T(z,\omega);\lambda]+\eta_R W_{eR}(\lambda)\}\epsilon(z,\lambda)\left(\exp\left[-\int_0^z \epsilon(z',\lambda)dz'\right]+R_b(\lambda)\left[\exp\left\{-\int_z^L \epsilon(z',\lambda)dz'\right\}+R_1(\lambda)\exp\left\{-\int_{-z}^L \epsilon(z',\lambda)dz'\right\}\right]\times\exp\left[-\int_0^L \epsilon(z',\lambda)dz'\right]\right)dz. \tag{19}$$

The various contributions to the emitted IR power can be separated out into background (dc) and harmonically varying components. Much work has been done in attempts to separate out carrier-wave and thermal-wave contributions through modulation frequency filtering,[2–5] however, they are always strongly mixed and can be separated out effectively only through spectral filtering at the IR detector. The various fields are

$$T_T(z,\omega)=T_0+\Delta T_T(z,\omega)e^{i\omega t}, \tag{20}$$

$$W_P[T_T(z,\omega);\lambda]=W_{P0}(T_0,\lambda)+\Delta W_P(z,\omega;\lambda)e^{i\omega t}, \tag{21}$$

$$\epsilon(z,\omega;\lambda)=\epsilon_0(\lambda)+\epsilon_{fc}(z,\omega;\lambda)e^{i\omega t}, \tag{22}$$

where T_0 is the ambient thermal-equilibrium temperature; also

$$\Delta T_T(z,\omega)=T_T(z,\omega)-T_0, \tag{23}$$

$$\Delta W_P(z,\omega;\lambda)=\frac{4h(c_0/n\lambda k_B T_0)A}{\exp(hc_0/\lambda n k_B T_0)-1}\left[\frac{\Delta T_T(z,\omega)}{T_0}\right], \tag{24}$$

and ϵ_0,ϵ_{fc} are the background IR emission coefficient and the component due to the free photoexcited CW, respectively. Through Kirchhoff's law, these quantities are equal to the background IR absorption coefficient α_{IR0} and the CW-related component α_{fc}, respectively. Both unmodulated emissive spectral powers per unit wavelength (Planck-mediated and direct radiative) can be conveniently grouped together:

$$W_0(T_0;\lambda)\equiv W_{P0}(T_0,\lambda)+\eta_R W_{eR}(\lambda). \tag{25}$$

According to Eq. (19) the ac component of the emission coefficient $\epsilon(z,\omega;\lambda)$ gives rise to an infinite series of terms of the form

$$\exp\left(-e^{i\omega t}\int_a^b \epsilon_{fc}(z,\omega;\lambda)dz\right)=1-e^{i\omega t}\int_a^b \epsilon_{fc}(z,\omega;\lambda)dz+\sum_{n=2}^{\infty}(-1)^n O(e^{in\omega t}), \tag{26}$$

which contains dc and linear terms, as well as an infinite series of (nonlinear) higher harmonics. Given that the typical PCR experimental configuration only involves lock-in demodulation of the fundamental and rejection of the dc and all higher harmonics, inserting the first two terms of expansion (26) into Eq. (19), retaining the terms proportional to $e^{i\omega t}$ only, and integrating over the semiconductor depth coordinate as well as over the detector spectral bandwidth, Eq. (16), results in an expression for the total emitted power at the fundamental frequency across the front surface of the material or the field of view of the IR detector, which ever is smaller:

$$P_T(\omega)=\int_{\lambda_1}^{\lambda_2} d\lambda[1-R_1(\lambda)]\left\{\epsilon_0(\lambda)\{1+R_b(\lambda)[1+R_1(\lambda)]\}\int_0^L e^{-\epsilon_0(\lambda)z}\Delta W_P(z,\omega;\lambda)dz+W_0(T_0;\lambda)\times\{1+R_b(\lambda)[1+R_1(\lambda)]\}\int_0^L e^{-\epsilon_0(\lambda)z}\epsilon_{fc}(z,\omega;\lambda)dz-\epsilon_0(\lambda)W_0(T_0;\lambda)\int_0^L e^{-\epsilon_0(\lambda)z}\left(\int_0^z \epsilon_{fc}(z',\omega;\lambda)dz'+R_b(\lambda)\times[1+R_1(\lambda)]\int_0^L \epsilon_{fc}(z',\omega;\lambda)dz'+R_b(\lambda)\left[\int_z^L \epsilon_{fc}(z',\omega;\lambda)dz'+R_1(\lambda)\int_{-z}^L \epsilon_{fc}(z',\omega;\lambda)dz'\right]\right)dz\right\}. \tag{27}$$

Further simplifications of this complicated expression can be made for lightly doped Si, in which the IR lattice absorption (and thus emission) coefficients are in the range of 1–2 cm^{-1}.[31] It is thus justified to set $e^{-\epsilon_0(\lambda)z}\sim 1$; $0\leqslant z \leqslant L$, where $L\sim 500\ \mu m$, for typical Si wafers. The effects of the breakdown of the approximation $\alpha_0 L \ll 1$ are investigated below (Sec. IV). The free-carrier absorption coefficient can be estimated by[32] $\alpha_{fc}=K_n\lambda^2\Delta N$ for n-type Si, where $K_n = 10^{-18}\ cm^2/\mu m^2$ and the maximum free-carrier density is $\Delta N \sim 10^{19}\ cm^{-3}$, limited by Auger recombinations. For p-type Si, $K_p\sim 2\times 10^{-18}\ cm^2/\mu m^2$. Calculation shows that $\alpha_{fc}\gg\alpha_0$ for photoexcited CW fields and intermediate injection conditions. Thus, it is easy to show that $(1+R_b(\lambda)[1+R_1(\lambda)])\int_0^L \epsilon_{fc}(z',\omega;\lambda)dz' \gg \epsilon_0(\lambda)\int_0^L dz \int_a^b \epsilon_{fc}(z',\omega;\lambda)dz'$ for all $a,b\in[0,L]$ and the third group of terms in Eq. (27) can be safely neglected compared to the second term, at least for application to Si. As a result, Eq. (27) can be simplified

$$P_T(\omega)\approx \int_{\lambda_1}^{\lambda_2} d\lambda[1-R_1(\lambda)]\{1+R_b(\lambda)[1+R_1(\lambda)]\} \times\left[\epsilon_0(\lambda)\int_0^L \Delta W_P(z,\omega;\lambda)dz + W_0(T_0;\lambda)\int_0^L \epsilon_{fc}(z,\omega;\lambda)dz\right]. \tag{28}$$

This expression shows that the presence of a backing support should increase the amplitude of the infrared signal by a factor of $1+R_b(\lambda)[1+R_1(\lambda)]$ compared to the free-standing sample. In Eq. (28), both terms in the brackets are oscillatory. The first term oscillates due to thermal-infrared emissions from the optically heated lattice and nonradiative deexcitations. The second term is oscillatory through the dependence of the absorption (equivalently, emission) coefficient on the free-carrier density[33]

$$\epsilon_{fc}(z,\omega;\lambda)=\alpha_{IRfc}(z,\omega;\lambda)=\frac{q\lambda^2}{4\pi^2\epsilon_{0D}c^3nm^{*2}\mu}\Delta N(z,\omega;\lambda), \tag{29}$$

for relatively low CW densities. Here, q is the elementary charge, ϵ_{0D} is the dielectric constant, c is the speed of light in the medium, n is the refractive index, m^* is the effective mass of the carrier (electron or hole), and μ is the mobility. This parameter is a function of donor or acceptor doping density and thus depends on $\Delta N(z,\omega;\lambda)$. The coherent oscillation of the free-carrier component of the IR absorption coefficient on account of the optical generation of carrier waves can act as an internal "chopper" for any incident external IR radiation, such as emissive power from a backing material.[34] To take into account the emissivity contributions of the backing material, we may assume a semiinfinite IR-opaque support in contact with, or at some short distance away from, the back surface of the semiconductor. From energy conservation $a(T_b,\lambda_b)+R_b(T_b,\lambda_b)=1$, where the subscript b indicates a backing material property. Using Kirchhoff's law, Eq. (5), it is easily deduced that

$$e(T_b,\lambda_b)=1-R_b(T_b,\lambda_b). \tag{30}$$

From the definition of emissivity, Eq. (4), the spectral emissive power from the backing is $W(T_b,\lambda_b) = W_P(T_b,\lambda_b)e(T,\lambda)$. On entering the back surface of the semiconductor, the density of thermally emitted IR photons at substrate temperature T_b will be periodically absorbed by the modulated CW and will emerge out of the front surface with a power

$$\Delta P_B(T_b,\omega;\lambda_b)=[1-R_1(\lambda_b)]W_P(T_b,\lambda_b)e(T_b,\lambda_b) \times\exp\left[-\int_0^L \alpha_{IR}(z,\omega;\lambda_b)dz\right], \tag{31}$$

where $R_2(\lambda_b)$ was assumed to be zero for matte surfaces. Use of Eq. (26) and retention of the fundamental component of the response only, yields the spectrally integrated backing emissivity contribution to the back-propagating IR power from the photoexcited semiconductor:

$$P_B(T_b,\omega)=-\int_{\lambda_1}^{\lambda_2} d\lambda_b W_P(T_b,\lambda_b)e(T_b,\lambda_b)[1-R_1(\lambda_b)] \times\int_0^L e^{-\epsilon_0(\lambda_b)z}\alpha_{IRfc}(z,\omega;\lambda_b)dz. \tag{32}$$

This expression assumes that the emissive power spectrum λ_b is within the spectral bandwidth of the IR detector. The negative sign indicates that the modulated transmitted radiation power across the front surface due to incident unmodulated thermal radiation from the backing is always out of phase with that generated internally due to CW recombination processes: The peak of the modulated component of the dc photon flux traveling across the semiconductor bulk will exit from the front surface, and thus appear at the detector, when the CW amplitude is low or zero, since it is then that the material IR transparency increases. Therefore, the IR emission flux from the backing is essentially out of phase with respect to the CW oscillation and tends to decrease the modulation depth of the CW emissions as compared to the absence of these backing emissions. Using the same approximations as with Eq. (28) and incorporating Eq. (32) into that equation, yields the complete expression for the total emitted power at the fundamental frequency across the front surface of the material in the presence of a backing support which acts both as reflector of the semiconductor-generated IR radiation with spectrum centered at λ and as emitter of backing-generated IR radiation centered at wavelength λ_b

$$P_T(\omega)\approx\int_{\lambda_1}^{\lambda_2} d\lambda[1-R_1(\lambda)]\Big\{\{1+R_b(\lambda)[1+R_1(\lambda)]\}\epsilon_0(\lambda) \times\int_0^L \Delta W_P(z,\omega;\lambda)dz+[\{1+R_b(\lambda)[1+R_1(\lambda)]\} \times W_0(T_0;\lambda)-W_P(T_b,\lambda)e(T_b,\lambda)[1-R_1(\lambda)]] \times\int_0^L \epsilon_{fc}(z,\omega;\lambda)\,dz\Big\}. \tag{33}$$

Even though the emission spectrum of the backing may clearly be different from that of the semiconductor itself, both contributions must be within the spectral bandwidth of the IR detector $[\lambda_1,\lambda_2]$ in Eq. (33). Therefore, by changing λ_b to λ it is assumed that only that portion of the two spectra that coincides with the detector bandwidth will be measured. The temperature of the backing support can also be different from that of the semiconductor, such as in the case of a heater. Equation (33) predicts that in the two extreme cases of a black absorber as a backing, with normal emissivity[35] $e(T_0,\lambda)\approx 1$ and $R_b\approx 0$, and of a metallic mirror with $e(T_0,\lambda)\approx 0$, Eq. (30), and $R_b\approx 1$, the expression in the curly bracket of total emitted power, Eq. (33), will become, respectively,

$$\epsilon_0(\lambda)\int_0^L \Delta W_P(z,\omega;\lambda)dz+\{W_0(T_0;\lambda)-W_P(T_b,\lambda)\times[1-R_1(\lambda)]\}\int_0^L \epsilon_{fc}(z,\omega;\lambda)dz \quad (\textit{black absorber}) \tag{34}$$

and

$$[2+R_1(\lambda)]\epsilon_0(\lambda)\int_0^L \Delta W_P(z,\omega;\lambda)dz +[2+R_1(\lambda)]W_0(T_0;\lambda)\int_0^L \epsilon_{fc}(z,\omega;\lambda)\,dz \quad (\textit{mirror}). \tag{35}$$

It is clear that a mirror backing will produce a stronger IR power emission than air backing, a prediction consistent with the earlier PTR experimental results[34] and with the PCR imaging results in this paper.

D. PCR of semiconductors with electronic damage or ion contamination

Photocarrier radiometry can be used as a CW imaging technique of electronically defective or impurity-ion-contaminated semiconductors. Focusing on the spectral bandwidth of the detector according to the requirement that the PCR signal spectral content should exclude Planck-mediated (thermal-infrared) photon capture, and that it should only involve direct radiative recombination IR photon emission, PCR can yield information about electronic defects in a semiconductor. In an electronic material with subsurface defects that affect the photoexcited carrier-wave density, or with impurity-ion-contamination regions that affect carrier recombination, the physical picture of IR photon emission in the affected region can be described in terms of the two separate signal-generation mechanisms, Planck-mediated and direct radiative IR photon emission. In a defective or contaminated semiconductor in the absence of photoinjected carrier waves, a uniform Planck emission dominates the IR photon flux at thermal equilibrium due to the uniform temperature of the semiconductor. The spectral emissive power centered around λ is $W_P(T_0;\lambda)d\lambda$, Eq. (3), and this function does not depend on optical or thermal properties of the semiconductor. In externally heated materials, it depends on the thermal properties only indirectly through the thermodynamic temperature T_0. Under conditions of no carrier injection, the IR absorption/emission coefficient at any wavelength λ in such a defective or contaminated semiconductor is a function of the coordinate (x,y,z) due to distributions of damage layers or contamination regions. The background absorption/emission coefficient becomes a function of the coordinate $\alpha_0(\lambda)\mapsto\alpha_0(\mathbf{r},\lambda)$. Under optical injection conditions, Planck-mediated emission due to optical absorption by the lattice or nonradiative decay in damaged or contaminated regions is different from that of intact material because the thermal properties are different, which affects the local temperature. The emissive power $\Delta W_P(z,\omega;\lambda)$, Eq. (24), in the affected region takes the form

$$\Delta W_{Pd}(z,\omega;\lambda)=W'_{P0}(T_0,\lambda)\Delta T_{Td}(z,\omega;\alpha_d)e^{i\omega t}, \tag{36}$$

where $W'_{P0}(T_0,\lambda)$ is a temperature derivative given by the expression multiplying $\Delta T_T(z,\omega)$ on the right-hand side of Eq. (24); the subscript d stands for "defect." α_d is the absorption coefficient of the affected region at the excitation wavelength, λ_{vis}. Its equivalent in the unaffected regions is symbolized by α. The injected CW from a modulated laser beam creates a modulated IR absorption/emission coefficient that differs in affected regions from other intact regions of the semiconductor. This occurs due to different optical absorption depths at the excitation wavelength, as well as different recombination rates in the affected regions. In the latter, the free-carrier-wave IR absorption coefficient is given by

$$\alpha_{IRfc,d}(z,\omega;\lambda,\alpha_d)=\frac{q\lambda^2}{4\pi^2\epsilon_{0D,d}c^3 n_d m^{*2}\mu_d}\Delta N_d(z,\omega;\lambda) \equiv C_d(\mathbf{r},\lambda)\Delta N_d(z,\omega;\alpha_d) \tag{37}$$

in the low-injection limit, where the mobility μ_d is independent of the doping density and under the assumption that the CW electronic properties $(n_d,\epsilon_{0D,d},\mu_d)$ are only mildly dependent on the coordinate. The intact material equivalent of this equation, Eq. (29), can be written as $\alpha_{IRfc}(z,\omega;\lambda,\alpha) =C(\lambda)\Delta N(z,\omega;\alpha)$. Therefore, the net IR power emitted from a defective or contaminated semiconductor is

$$P_{Td}(\omega)=\int_{\lambda_1}^{\lambda_2}d\lambda\int_0^L dP_d(z,\omega;\lambda), \tag{38}$$

replacing Eq. (16). Taking into account the arbitrary spatial dependencies of the electronic parameters in the affected region, retaining only terms $\propto e^{i\omega t}$, ignoring lateral variations across the semiconductor (i.e., assuming only depth distributions of defects/impurities leading to one-dimensional geometry) and using Eq. (36), it is found that Eq. (28) must be replaced by

$$P_{Td}(\omega)\approx\int_{\lambda_1}^{\lambda_2}[1-R_1(\lambda)]\{1+R_b(\lambda)[1+R_1(\lambda)]\}\times\left[W'_{P0}(T_0,\lambda)\int_0^L\epsilon_{0d}(z,\lambda)\Delta T_{Td}(z,\omega;\epsilon_{0d})dz+\int_0^L C_d(z,\lambda)W_{0d}(z,T_0;\lambda)\Delta N_d(z,\omega;\epsilon_{0d})dz\right]d\lambda, \tag{39}$$

where the harmonic dependence $e^{i\omega t}$ is implied and

$$W_{0d}(z,T_0;\lambda)\equiv W_{P0}(T_{0d},\lambda)+\eta_{Rd}(z)W_{eRd}(z,\lambda). \tag{40}$$

A particularly useful and compact version of Eq. (33) for intact (homogeneous) semiconductors, incorporating Eq. (29) for the free-carrier-wave emission coefficient, and separating out spatial and modulation-frequency contributions from spectral contributions is given by

$$P_T(\omega)\approx F_1(T_0;\lambda_1,\lambda_2)\int_0^L\Delta T_T(z,\omega)\,dz+F_2(T_0;\lambda_1,\lambda_2)\int_0^L\Delta N(z,\omega)\,dz, \tag{41}$$

with the definitions

$$F_1(T_0;\lambda_1,\lambda_2)\equiv\int_{\lambda_1}^{\lambda_2}[1-R_1(\lambda)]\{1+R_b(\lambda)\times[1+R_1(\lambda)]\}W'_{P0}(T_0,\lambda)d\lambda, \tag{42}$$

$$F_2(T_0;\lambda_1,\lambda_2)\equiv\int_{\lambda_1}^{\lambda_2}[1-R_1(\lambda)]\{1+R_b(\lambda)\times[1+R_1(\lambda)]\}W_0(T_0;\lambda)C(\lambda)d\lambda. \tag{43}$$

It is understood that integration over λ must be performed after the spatial integrations are completed. An equation similar to Eq. (41) can also be written for the region with subsurface defects. These expressions must be used in conventional PTR of electronic solids. For spectrally selective PCR, a simplified nonthermal signal expression can be written using Eq. (33), through elimination (filtering) of all thermal-infrared emission contributions:

$$P(\omega)\approx\int_{\lambda_1}^{\lambda_2}d\lambda[1-R_1(\lambda)]\{1+R_b(\lambda)\times[1+R_1(\lambda)]\}\eta_R W_{eR}(\lambda)\int_0^L\epsilon_{fc}(z,\omega;\lambda)dz. \tag{44}$$

Also, instead of Eqs. (41)–(43), the following PCR expressions are derived in one dimension:

$$P(\omega)\approx F_2(\lambda_1,\lambda_2)\int_0^L\Delta N(z,\omega)\,dz, \tag{45}$$

with

$$F_2(\lambda_1,\lambda_2)\equiv\int_{\lambda_1}^{\lambda_2}[1-R_1(\lambda)]\{1+R_b(\lambda)\times[1+R_1(\lambda)]\}\eta_R W_{eR}(\lambda)C(\lambda)d\lambda. \tag{46}$$

Similar expressions with straightforward changes can be used for semiconductors with electronic defects or contamination.

III. PCR IMAGING OF ELECTRONIC DEFECTS IN SI WAFERS

A. Instrumentation and signal characteristics

The experimental implementation of laser infrared photocarrier radiometry is similar to the typical PTR setup for semiconductors,[4–9] with the crucial difference being that the spectral window of the IR detector and/or optical filter, and the modulation-frequency response of the preamplifier stage, must be tailored through spectral bandwidth matching to a combination of carrier recombination emissions and effective filtering of the Planck-mediated thermal-infrared emission band. Conventional PTR utilizes photoconductive liquid-nitrogen-cooled HgCdTe (MCT) detectors with spectral bandwidth in the 2–12 μm range. This includes the thermal-infrared range, 7–12 μm, and only part of the electronic emission spectrum at shorter wavelengths. Unfortunately, the spectral detectivity responses of MCT detectors are heavily weighed toward the thermal-infrared end of the spectrum.[36] The result is an infrared signal with unequal superposition of recombination and thermal emission responses with a larger weight of the thermal-infrared component. From preliminary experiments with several IR detectors and bandpass optical filters, we concluded that emissive infrared radiation from electronic CW recombination in Si is centered mainly in the spectral region below 3 μm.[37] Among those, InGaAs detectors with integrated amplifiers, a visible radiation filter and a spectral response in the $<$1800-nm range, were found to be most suitable, exhibiting 100% efficient filtering of the thermal-infrared emission spectrum from Si as well as maximum signal-to-noise ratio over InGaAs detectors with separate amplifiers and InAs detectors. Therefore, infrared PCR was introduced using an optimally spectrally matched room-temperature InGaAs photodetector (Thorlabs model PDA255) for our measurements, with a built-in amplifier and frequency response up to 50 MHz. The active element area was 0.6 mm^2 with a spectral window in the 600–1800 nm range with peak responsivity 0.95 A/W at 1650 nm. The incident Ar-ion laser-beam size was 1.06 mm and the power was 20–24 mW. The detector was proven extremely effective in cutting off all thermal-infrared radiation: Preliminary measurements using nonelectronic materials (metals, thin foils, and rubber) showed no responses whatsoever. Comparison with conventional PTR results was made by replacing the InGaAs detector with a Judson Technologies liquid-nitrogen-cooled model J15D12 MCT detector covering the 2–12 μm range with peak detectivity 5×10^{10} cmHz$^{1/2}$ W^{-1}. Figure 3 shows two frequency re-

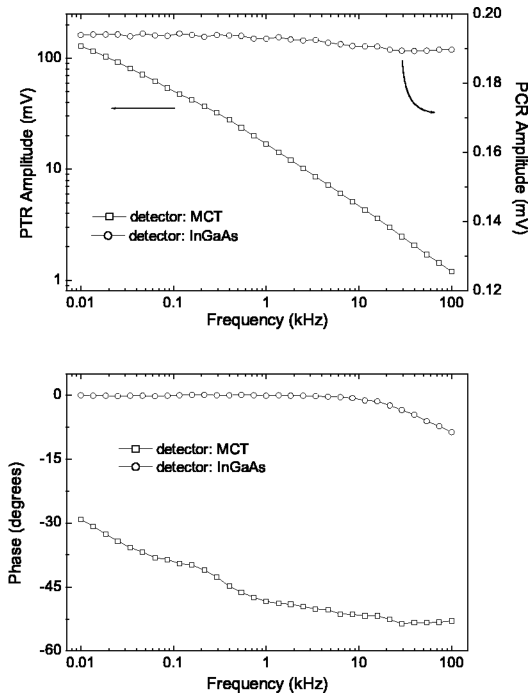

FIG. 3. Comparison of the normalized PTR (MCT detector) and PCR (InGaAs detector) signals from an AlGaAs quantum well array on a GaAs wafer. Incident laser power: 25 mW.

sponses from a test AlGaAs quantum well array on GaAs substrate using both the MCT and the InGaAs detectors. The MCT response is characteristic of thermal-wave domination of the PTR signal throughout the entire modulation-frequency range of the lock-in amplifier. On the other hand, the PCR signal from the InGaAs detector/preamplifier exhibits very flat amplitude, characteristic of purely carrier-wave response and zero phase lag up to 10 kHz, as expected from the oscillation of free carriers in phase with the optical flux which excites them (modulated pump laser). The apparent high-frequency phase lag is associated with electronic processes in the sample. The PTR signals were normalized for the instrumental transfer function with the thermal-wave response from a Zr alloy reference, whereas the PCR signals were normalized with the response of the InGaAs detector to a small fraction of the exciting modulated laser source radiation at 514 nm. Regarding the well-known nonlinearity of the PTR signals with pump laser power,[38] Fig. 4 shows a nonlinear response from the PTR system at laser powers $\gtrsim 5$ mW. The PCR system, however, exhibits a fairly linear behavior for powers >15 mW and up to 35 mW, within the range of the present experiments.

Unlike the readily available thermal-infrared emissions from well-controlled reference samples for the purpose of instrumental signal normalization in semiconductor PTR,[39] the quest for suitable reference samples for PCR is a much more difficult problem because of the absence of detector response in the thermal-infrared spectral region. Furthermore, the foregoing normalization procedure using a small fraction of the excitation laser beam is error prone, as the InGaAs detector is extremely sensitive to light intensity and its wavelength and tends to exhibit nonlinear behavior.

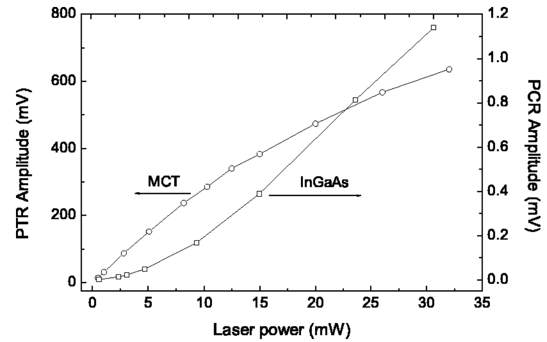

FIG. 4. The PCR and PTR signal dependencies on the power of the excitation Ar-ion laser. The sample was a p-type Si wafer of resistivity $\rho \sim 20\ \Omega$ cm. Both phases were essentially constant within the 0–35 mW range.

Therefore, an indirect normalization method was introduced as shown in Fig. 5. Frequency scans on a Si wafer with a large degree of signal variation across its surface were obtained from two such locations with very different responses, using both the MCT and the InGaAs detectors. Then the amplitude ratios and phase differences between the two locations using the same detector were plotted and the amplitude ratios were further normalized at 100 kHz, Fig. 5(a). These self-normalized data are independent of the instrumental transfer function and depend only on differences among electronic parameters (PCR) or combinations of thermal and electronic parameters (PTR) at the two coordinate locations. Upon superposition of the self-normalized signals it was found that both amplitude and phase curves essentially over-

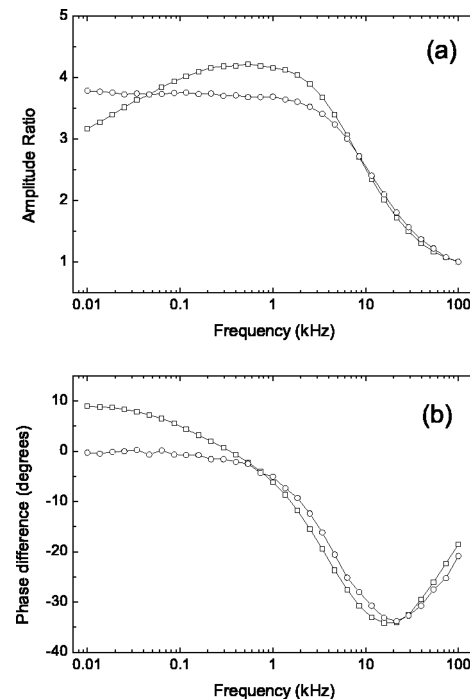

FIG. 5. (a) Self-normalized PTR and PCR signal amplitudes and (b) phases from two locations on an inhomogeneous n-type Si wafer using 20-mW Ar-ion laser and 1.2-mm beam size. $-\square-\square-$, PCR technique; $-O-O-$, PTR technique.

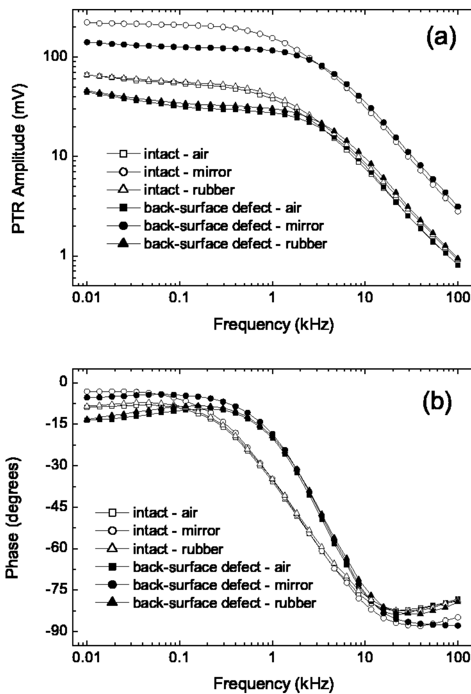

FIG. 6. The PTR frequency scans from the *p*-type Si wafer of Fig. 4 in air and with two backing supports. Laser-beam power 25 mW. (a) Amplitudes and (b) phases.

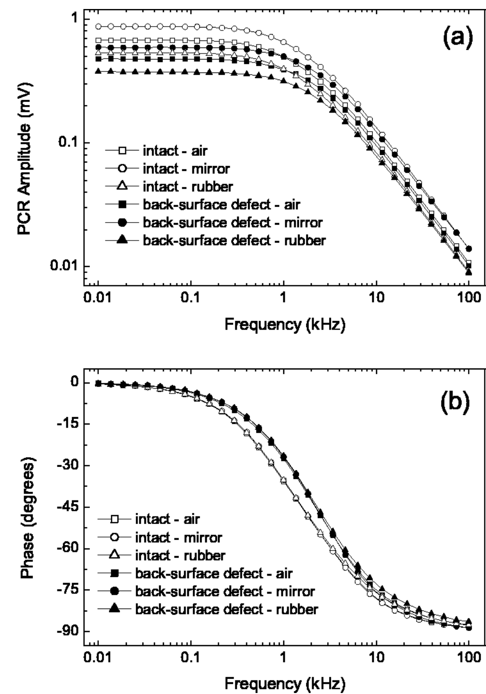

FIG. 7. The PCR frequency scans from the same *p*-type Si wafer with air and two backing supports. Laser-beam power 25 mW. (a) Amplitudes and (b) phases.

lapped within the electronic region. This implies that both detectors monitor the same electronic CW phenomena at high frequencies and thus the instrumental normalization of the PCR signal can be performed by (1) using the PTR signal from a high-electronic-quality reference Si wafer, normalized by a simple one-dimensional thermal-wave frequency scan of a homogeneous metallic solid;[5] (2) mathematically extracting the electronic component of the PTR signal[5] and adjusting the PCR signal to this component; and (3) using the PCR amplitude and phase frequency correction functions for all other signal normalizations. This indirect scheme was proven satisfactory. It will be seen in Sec. IV, however, that the small differences in the self-normalized high-frequency signals of Fig. 5 are indicative that the thermal-wave component of the PTR signal can be present even at the highest modulation frequencies and, without independent knowledge of the electronic properties of the reference semiconductor, it can affect their "true" values significantly, a conclusion we also reached about photomodulated thermoreflectance.[21]

B. Effects of backing material

A small area of the back surface of the Si wafer which was used for the signal linearity studies was very slightly damaged through gentle rubbing with sandpaper. The PTR and PCR frequency scans were obtained from outside and inside the region with the back-surface defect. Then line scans and two-dimensional images at fixed frequency were obtained covering the defect area. The wafer was suspended in air using a hollow sample holder, or was supported by a black rubber or by a mirror backing. Figure 6 shows the PTR frequency scans for all three backings. The strongest signal amplitude is generated with the mirror backing in both intact and defective regions. Air and rubber backings yield very similar signals. Figure 7 shows the PCR responses that indicate similar trends, but the PCR technique resolves the amplitudes from the three backings in the order $S_M > S_A > S_R$, (M mirror, A air, R rubber). To understand the origins of the signal changes in the presence of a backing support, a highly reflecting aluminum-foil-covered backing was placed at a variable distance from the back surface of the Si wafer across from an intact region and the PTR and PCR signals were monitored, Fig. 8. It is observed that the PCR amplitude remains constant for all three frequencies up to a distance of $\sim$1 mm away from contacting the back surface, where it starts to increase. The curves are normalized to their value on the surface to show that the rate of increase is independent of frequency. The PCR phase remains essentially flat throughout. On the other hand, the PTR amplitude monotonically increases with decreasing distance from the back surface. The rate of increase changes slope $\sim$2 mm away from the surface, a transition region where the phase also changes. Similar experiments with the mechanically damaged area replacing the intact surface resulted in very similar behavior. The PTR signal order with various backings observed in Fig. 6 is in agreement with measurements performed by Sheard and Somekh.[34] To determine the origin of the PTR and PCR signal variations with backing (whether due to IR photon internal reflections or backing emissivity changes[34]), the laser beam was turned off and a mechanical chopper was placed at some distance away from the IR detector. Lock-in amplifier signals from the MCT detector using the same three Si-substrate interfaces were observed as follows: Mirror backing, 2.0 V; air backing, 1.88 V; black rubber backing, 1.86 V; bare rubber or mirror with no overlying Si sample, 1.95 V. These values were greatly influenced by the emissiv-

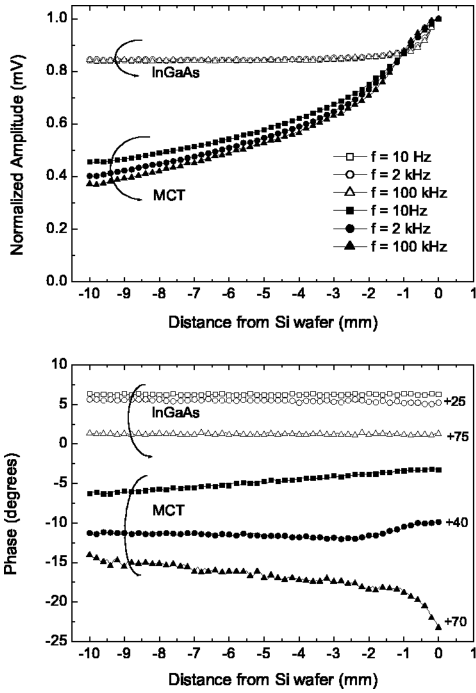

FIG. 8. The PCR and PTR distance scans between an intact back-surface region of the Si wafer and a highly reflective aluminum foil-covered substrate. All amplitude curves have been normalized to unity at the wafer back surface; phase curves indicate the offset (in degrees) of the experimental phase for convenience in grouping. Laser power: 24 mW.

ity of the mechanical chopper itself as deduced by the strong dependence of the signal on the chopper position. Replacing the MCT with the InGaAs detector, the signal nearly vanished at $\sim 5\ \mu$V, a baseline value that remained constant for all combinations of wafer, chopper, and substrates. Regarding the PTR signals and given that for opaque materials $e(T_b,\lambda_b)=1-R_b(T_b,\lambda_b)$, Eq. (30), it is not immediately evident whether the signal enhancement at close proximity of the substrate to the sample in Fig. 8 may be due to transmitted substrate dc thermal-infrared emissivity, modulated by the harmonically varying IR emission coefficient of the Si wafer, or may be due to direct-recombination-emitted and substrate-reflected modulated IR photons from inside the Si wafer. The fact that both amplitude and phase PTR signals from rubber and air (no reflection) are almost identical, Fig. 6, and the approximate normal emissivities are $\simeq 1$ for air and $\simeq 0.86$ for black rubber (Ref. 35, p. 531) supports the hypothesis of Sheard and Somekh that the PTR signal enhancement with a mirror (normal emissivity $\leqslant 0.04$ (Ref. 35 p. 531) is due to the dc emissivity of the backing. This is further corroborated by the PTR behavior shown in Fig. 8, the monotonic increase of which can be understood in terms of the transmission of IR emissive photons within an increasing solid angle subtended by the MCT detector to the other side of the wafer. On the other hand, the dc emissivity experiments with the InGaAs detector in place are clear evidence that its spectral bandwidth lies entirely outside the thermal IR (Planck) emission range of the Si wafer with or without substrate. Therefore, the PCR amplitude enhancement for mirrored and rubber backings, Fig. 7(a), is consistent with simple reflection of exiting (transmitted) CW-generated IR photons at the surface of the backing, with no possibility for thermal-infrared emissivity contributions from the backing itself. The order of the PCR amplitude curves indicates that the surface of highest reflectivity (mirror) yields the strongest signal. Apparently, the Si-air interface is a more efficient backscatterer of IR photons than the Si-black rubber interface, where these photons are expected to be more readily absorbed by the rubber. From Eq. (44) it is expected that the ratio of the PCR signals with mirror and black rubber backings should be approximately $[2+R_1(\lambda)]/(1+R_b(\lambda)[1+R_1(\lambda)])\approx 1.94$. The measured ratio from the low-frequency end in Fig. 7(a) is 1.8. The PCR signal dependence on the distance ($\leqslant 1$ mm) between sample and substrate indicates that substrate-reflected IR photons exiting from the sample itself contribute to the observed PTR signal enhancement, an effect not foreseen in the hypothesis of Sheard and Somekh. This additional source of the PTR signal is likely to be responsible for the change in the PTR amplitude slope and phase shift at distances <2 mm observed in Fig. 8.

C. PCR imaging of deep subsurface electronic defects

Figure 9 shows line scans with the excitation laser-beam scanning the front (polished) surface of a 20-Ωcm p-type Si wafer and the IR detector on the same side. Based on the backing results, for maximum signal strength the sample was resting on a mirror. Both the PTR and PCR amplitude and phase scans were obtained and both show sensitivity to the deep defect on the back-surface scratched region. However, at 100-kHz imaging can be performed only with the PCR signal. At all three selected modulation frequencies, the PCR amplitude decreases when the laser-beam scans over the defect region, consistent with the expected CW density decrease as the back-surface defect efficiently traps carriers and removes them from further diffusion and potential radiative recombination. The PCR phase scan remains essentially constant at 10 Hz, Fig. 9(b), as the diffusion-wave centroid is solely determined by the ac carrier-wave-diffusion length[14]

$$L_{ac}(\omega)=\sqrt{\frac{D^*\tau}{1+i\omega\tau}}, \tag{47}$$

where τ is the lifetime and D^* is the ambipolar carrier-diffusion coefficient. This particular wafer was measured to have $\tau\simeq 1$ ms and $D^*\simeq 12\ \mathrm{cm^2/s}$, which yields an $|L_{ac}(10\ \mathrm{Hz})|\simeq 1.1$ mm. Therefore, the CW centroid lies well beyond the thickness of the wafer ($\sim 630\ \mu$m) and no phase shift can be observed. At the intermediate frequency of 1360 Hz, $|L_{ac}|\simeq 373\ \mu$m, well within the bulk of the wafer. In this case, a phase lead appears within the defective region. This occurs because the CW spatial distribution across the body of the wafer in the defective region is weighed more heavily toward the front surface on account of the heavy depletion occurring at, and near, the back surface. As a result, the CW centroid is shifted toward the front surface, manifested by a phase lead. Finally, at 100 kHz, $|L_{ac}|\simeq 44\ \mu$m. Nevertheless, Fig. 9(a) shows that there is still PCR amplitude con-

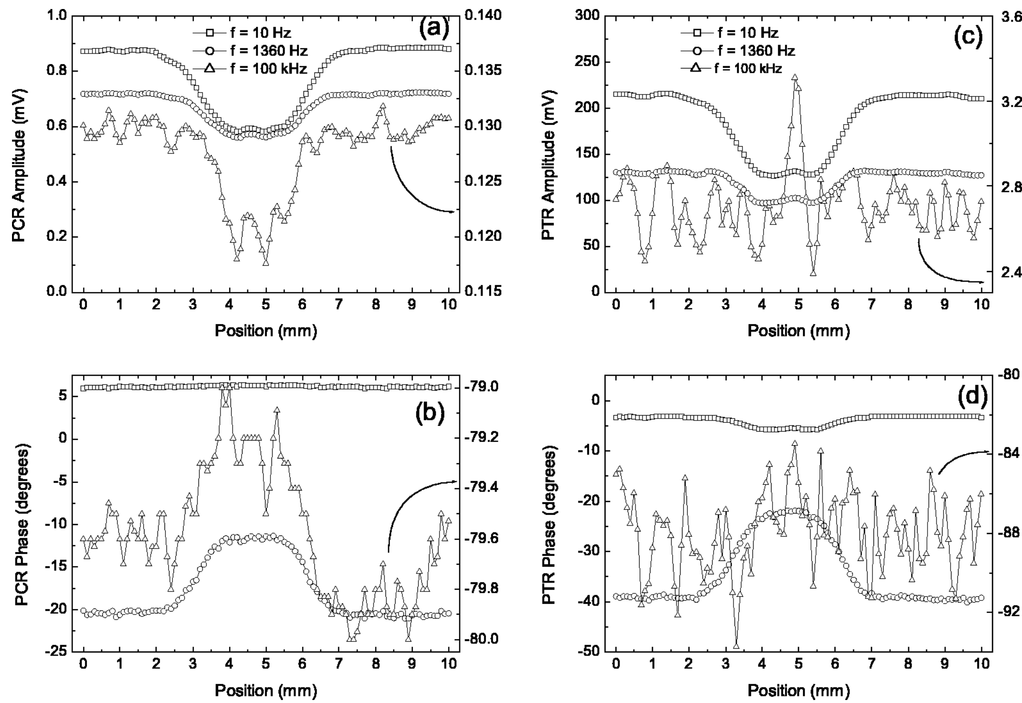

FIG. 9. Line scans over a p-Si wafer region with back-surface mechanical damage. (a) PCR amplitude; (b) PCR phase; (c) PTR amplitude; and (d) PTR phase. The wafer is resting on a mirror support. Laser power: 24 mW.

trast at that frequency, accompanied by a small phase lead, Fig. 9(b). For the PTR scans, Fig. 9(c) shows that the overall amplitude is controlled by the CW component at 10 and 1360 Hz, and there is a small contrast at 100 kHz. The PTR phase contrast within the region with the back-surface defect first appears as a lag at the lowest frequency of 10 Hz, as expected from a shift away from the front surface of the diffusion-wave centroid in the presence of a remote thermal-wave source which is added to the combined PTR signal. At that frequency, the thermal-wave diffusion length[14] is $L_t(\omega)=\sqrt{2D_t/\omega}\simeq 1.7$ mm, that is, the back surface is in thermal conductive communication with the front surface. Therefore, the thermal wave, rather than the carrier wave, controls the overall diffusion-wave PTR behavior of the Si wafer at 10 Hz. At 1360 Hz, however, $L_t\simeq 148$ μm, therefore, there is no thermal contact with the back surface. The only signal component affected by the remote defect is the CW, and the phase behaves as in the PCR case, exhibiting a net lead within the defective region. At 100 kHz there is no PTR phase sensitivity to the defect; only a vestigial amplitude contrast, Figs. 9(c,d). To maximize the PCR and PTR imaging contrast, differences in amplitudes and phases as a function of frequency were obtained outside and inside the defective region. It is with the help of this type of analysis that the 1360 Hz frequency was chosen for both techniques as one with the highest contrast in phase (but not in amplitude). It is clear that while the PTR contrast is generally higher at low frequencies due to the cooperative trends in both thermal-wave and carrier-wave components, however, the PCR imaging contrast becomes superior above ca. 1 kHz and retains its contrast even at the highest frequency of 100 kHz. Figure 10 shows images of the back-surface defect obtained through front-surface inspection using both techniques at the optimum contrast frequency of 1360 Hz. Figure 11 shows the same scan at 100 kHz. At this frequency, the PTR image is dominated by noise and is unable to produce any contrast between the intact and defective regions, wheras the PCR image clearly shows the highest spatial resolution of the back-surface defect possible. The PCR phase, Fig. 11(b), shows details of the central defect as well as the radially diverging defect structures at the base of the central defect, such as a ''zoomed in'' version of the 1360 Hz image, Fig. 10(b). Both the PCR images clearly reveal internal substructure of the central defect, which was invisible at 1360 Hz. In a manner reminiscent of conventional propagating wave fields, image resolution increases with decreasing carrier wavelength, $|L_{ac}(\omega)|$. Similar images to Figs. 10 and 11 were obtained with air or rubber backing of the same wafer, with marginally diminished detail and contrast. The contrast for the PCR phase imaging at 100 kHz, Fig. 11(b), is about 11% for amplitude [Fig. 9(a)], while the phase difference is only 1° [Fig. 9(b)]. The very high sensitivity of the PCR imaging to defect identification is apparent: despite this very small variation in phase, the defect can be clearly delineated. In the case of PTR at 100 kHz, the contrast for amplitude is about 28% [taking the sharp peak in Fig. 9(c) into account]. The phase difference is about 10°. An examination of Figs. 9(c) and 9(d) at 100 kHz shows that this ''higher contrast'' is caused by fluctuations of the signal, as the PTR signal-to-noise ratio (SNR) is relatively poor, resulting in the disappearance of the back-surface defect from the images Figs. 11(c,d). The PCR images exhibit much higher SNR and clearly reveal the defect structure.

Under front-surface inspection and precise depth profilometric control by virtue of the PCR modulation-frequency-adjustable carrier-wave-diffusion length, Eq. (47), Figs. 10

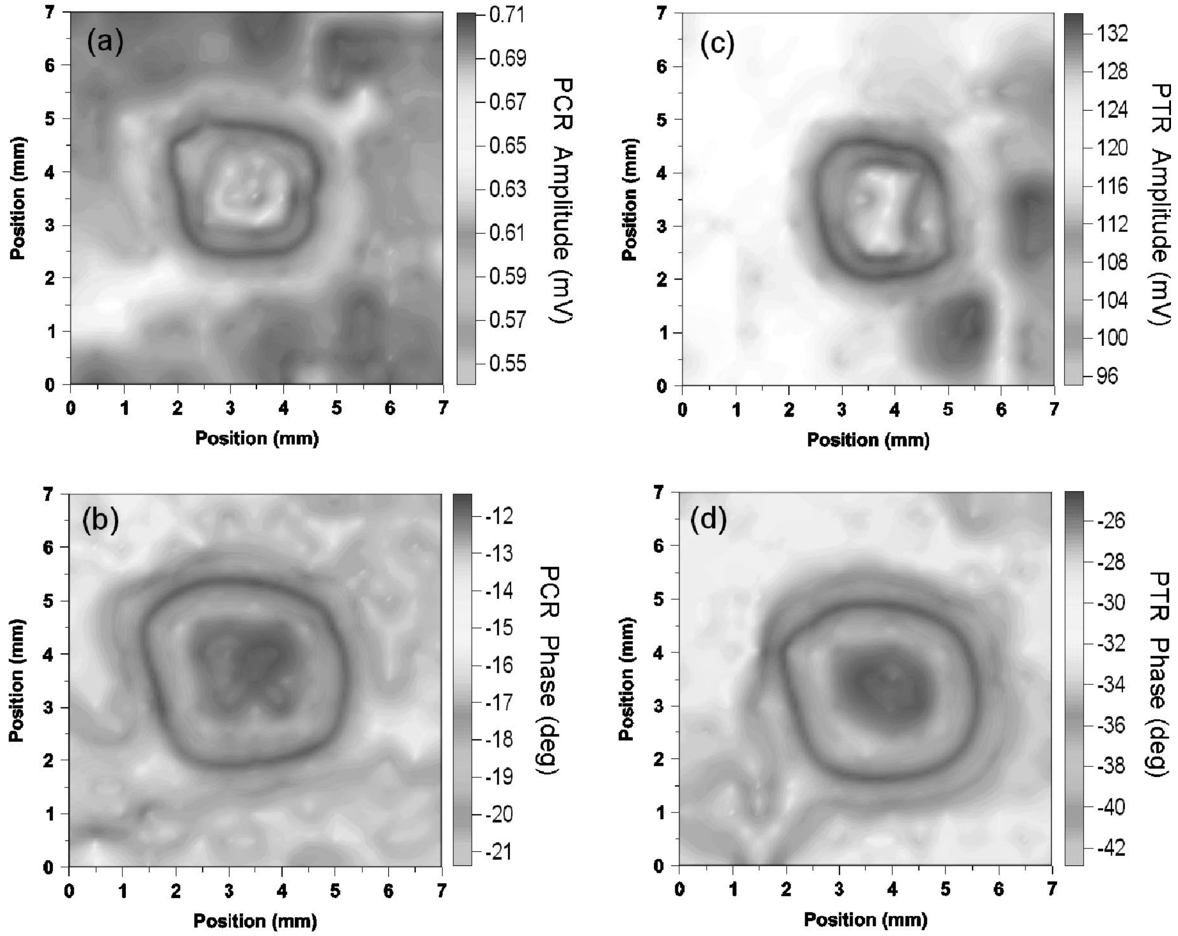

FIG. 10. Scanning imaging of back-surface defect in the p-Si wafer using front-surface inspection. Laser beam radius, 518 μm. Frequency, 1360 Hz. (a) PCR amplitude; (b) PCR phase; (c) PTR amplitude; and (d) PTR phase.

and 11 show that with today's high-quality, long-lifetime industrial Si wafers, one can observe full images of sharp carrier-wave density contrast due to underlying defects very deep inside the bulk of a Si wafer. Specifically, high-frequency PCR imaging reveals so far unknown very long-range effects of carrier interactions with deep subsurface defect structures and the detrimental ability of such structures to decrease the overall free photoexcited-carrier density far away from the defect sites at or near the front surface where device fabrication takes place. This phenomenon may be important toward device fabrication improvement through careful selection of substrate wafers with regard to deep bulk growth and manufacturing defects that were heretofore not associated with device performance. Further, the PCR imaging experiments with shorter lifetime Si wafers have shown that it may be beneficial to use lower quality starting substrates in order to avoid the full effects of deep subsurface defects on the electronic quality of the upper (device-level) surface.

IV. QUANTITATIVE PCR MEASUREMENTS OF ELECTRONIC TRANSPORT PROPERTIES

The structure of Eq. (27), the expression for the total emitted power from a semiconductor crystal at the fundamental frequency across the field of view of the IR detector, shows depth dependence of the spatial integrals on the equilibrium IR emission coefficient $\epsilon_0(\lambda)$ of the semiconductor. If this parameter is larger than 1–5 cm^{-1}, it introduces a weighting factor $e^{-\epsilon_0(\lambda)z}$ under the integral signs of the compact expression for the total IR emission, Eq. (41), as well as for the pure PCR emission, Eqs. (44)–(46). To estimate the effect of such a factor on the PCR signal, especially in the case of low-resistivity, high-residual infrared absorption Si wafers, a simulation was performed using the PCR Eqs. (45) and (46) in the three-dimensional (3D) form

$$P(r,\omega;\lambda_1,\lambda_2)\approx\int_{\lambda_1}^{\lambda_2}[1-R_1(\lambda)]\{1+R_b(\lambda)\times[1+R_1(\lambda)]\}\eta_R W_{eR}(\lambda)C(\lambda)d\lambda\times\int_0^L \Delta N(r,z,\omega)e^{-\epsilon_0(\lambda)z}dz. \tag{48}$$

The equation for $\Delta N(r,z,\omega)$, the 3D extension of $\Delta N(z,\omega)$ is the solution to the photocarrier-wave boundary-value problem. It was obtained from Ref. 14, Chap. 9, Eq. (9.106), and it is reproduced here

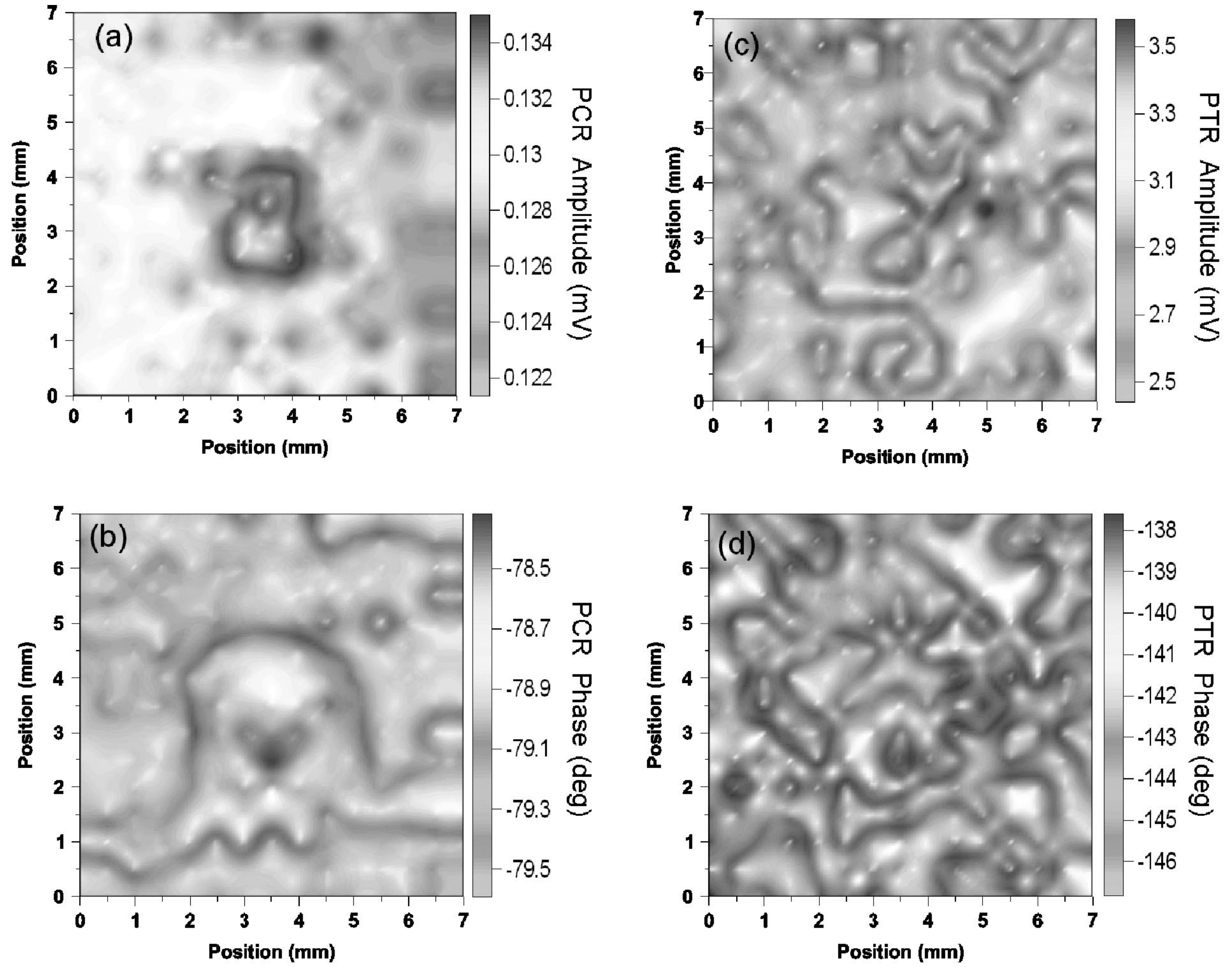

FIG. 11. Scanning imaging of back-surface defect in the p-Si wafer using front-surface inspection. Laser beam radius, 518 μm. Frequency, 100 kHz. (a) PCR amplitude; (b) PCR phase; (c) PTR amplitude; and (d) PTR phase.

$$\Delta N(r,z,\omega)=\frac{\eta_Q P_0 \alpha}{2\pi h\nu D^*}\int_0^\infty \frac{e^{-k^2W^2/4}}{(\alpha^2-\xi_e^2)}\times\Bigg[\left(\frac{G_2 g_1-g_2 G_1 e^{-(\xi_e+\alpha)L}}{G_2-G_1 e^{-2\xi_e L}}\right)e^{-\xi_e z}-e^{-\alpha z}+\left(\frac{g_1-g_2 e^{-(\alpha-\xi_e)L}}{G_2-G_1 e^{-2\xi_e L}}\right)\times e^{-\xi_e(2L-z)}\Bigg]J_0(kr)k\,dk, \quad (49)$$

where

$$g_1(k)\equiv\frac{D^*\alpha+S_1}{D^*\xi_e(k)+S_1};\quad g_2(k)\equiv\frac{D^*\alpha-S_2}{D^*\xi_e(k)-S_2};\quad (50)$$

with

$$G_1(k)\equiv\frac{D^*\xi_e(k)-S_1}{D^*\xi_e(k)+S_1};\quad G_2(k)\equiv\frac{D^*\xi_e(k)+S_2}{D^*\xi_e(k)-S_2};\quad (51)$$

and

$$\xi_e(k)\equiv\sqrt{k^2+\sigma_e^2}. \quad (52)$$

Here, k stands for the Hankel variable of radial integration, W is the Gaussian laser-beam spotsize, S_1 and S_2 are the front- and back-surface recombination velocities, L is the thickness of the semiconductor slab, α is the optical absorption coefficient at the excitation wavelength $\lambda_{vis}=c_0/\nu$. η_Q is the quantum yield for optical to electronic energy conversion and P_0 is the laser power. The carrier-wave number is defined as

$$\sigma_e(\omega)\equiv\sqrt{\frac{1+i\omega\tau}{D^*\tau}}=\frac{1}{L_{ac}(\omega)}. \quad (53)$$

In the simulations that follow and in the theoretical fits to the experimental data, the variable r was integrated over the surface of the IR detector.[4]

Figure 12 shows simulations of the PCR frequency dependence for p-Si of (what amounts to) different resistivity with the equilibrium IR absorption coefficient as a IR-wavelength-independent (average) parameter. From Kirchhoff's law and Eq. (22), $\epsilon_0=\alpha_{IR0}$. The curves show a de-

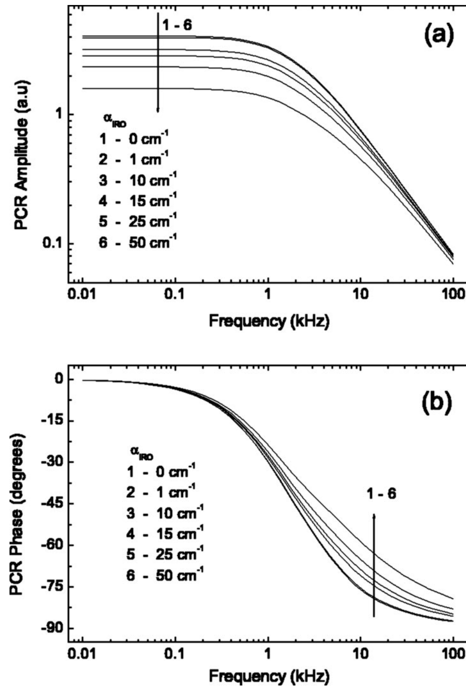

FIG. 12. Simulations of the PCR signal frequency dependence in p-Si with the residual IR absorption coefficient as a parameter. (a) Amplitude; (b) phase $\lambda=514$ nm, beam radius $W=518$ μm, detector radius $=563$ μm, wafer thickness $=675$ μm; $\tau=1$ ms, $D^*=15$ cm^2/s, $S_1=100$ cm/s, $S_2=300$ cm/s.

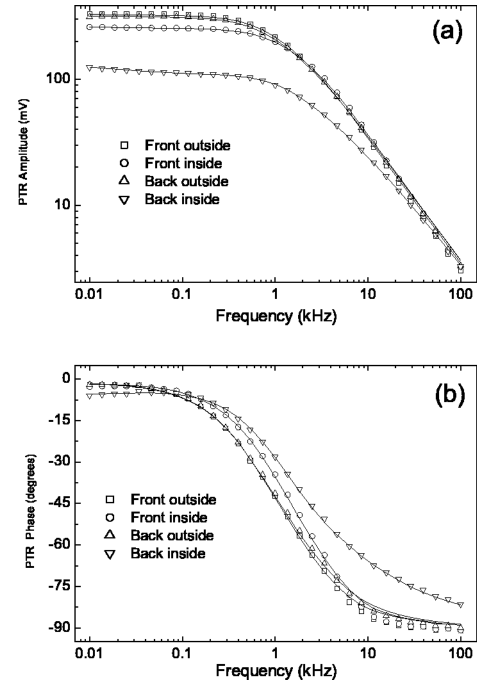

FIG. 13. Front- and back-surface PTR frequency scans inside and outside a defect area of a p-Si wafer on aluminum backing. Detector, MCT; beam size, 1.4 mm; Ar-ion laser power, 20 mW. (a) Amplitudes and (b) phases. Best fit parameters. Front intact region: $\tau=1$ ms, $D^*=12$ cm^2/s; $S_1=10$ cm/s; $S_2=210$ cm/s; $C_p=9\times10^{-16}$ (a.u.); $C_t=5\times10^6$ (a.u.). Front inside the defect: $\tau=1$ ms, $D^*=15$ cm^2/s; $S_1=10$ cm/s; $S_2=450$ cm/s; $C_p=9.5\times10^{-16}$ (a.u.); $C_t=5\times10^6$ (a.u.). Back intact region: $\tau=1$ ms, $D^*=13.2$ cm^2/s; $S_1=45$ cm/s; $S_2=650$ cm/s; $C_p=9\times10^{-16}$ (a.u.); $C_t=5\times10^6$ (a.u.). Back inside the defect: $\tau=1$ ms, $D^*=14.5$ cm^2/s; $S_1=650$ cm/s; $S_2=25$ cm/s; $C_p=1\times10^{-16}$ (a.u.); $C_t=8.5\times10^6$ (a.u.).

crease in amplitude, especially at low frequencies, in the carrier-diffusion-wave thin regime ($|L_{ac}(\omega)|>L$), as emissions throughout the bulk of the crystal are gradually impeded with increasing background carrier density (and thus IR absorption coefficient) due to self-absorption of the IR recombination photons by the background free-carrier-wave density. At high frequencies, in the carrier-diffusion-wave thick regime ($|L_{ac}(\omega)|\ll L$), little attenuation of the backward emitted IR recombination photon flux occurs because the IR-opaque subsurface layer involved in the CW-generated emission is very thin. Therefore, all amplitude curves converge. The PCR phase lags show sensitivity at high frequencies; they decrease with increasing frequency because the contributing CW centroid moves closer to the front surface with increasing IR opacity of the semiconductor. Figure 12 shows that for typical α_{IR0} ranges[31] of 1–2 cm^{-1} the effect of self-reabsorption of IR photons due to background free-carrier-wave densities is minimal and therefore the approximate Eqs. (28), (33), (41), (44), (45), and (46) are justified. The PCR image contrast of Figs. 10 and 11 can, in principle, be quantified by use of the CW term in Eq. (41), appropriately modified to accommodate the defective region:

$$\Delta P(\omega)\approx F_2(\lambda_1,\lambda_2)\left[\int_0^L \Delta N(z,\omega)dz-\int_0^L \Delta N_d(z,\omega)dz\right], \tag{54}$$

where $\Delta P(\omega)$ is the difference in signal between the intact and defective regions. This is a complex quantity, so it can be separated out into amplitude and phase components. The apparent simplicity of this expression is due to the fact that the subsurface defects considered here are on the back surface of the wafer and their presence mostly impacts the value of S_2 in Eq. (49), while the bulk parameters and the terms comprising the prefactor $F_2(\lambda_1,\lambda_2)$, Eq. (46), remain essentially unaltered, including $C_d(\lambda)\approx C(\lambda)$ for a thin damage layer in an otherwise homogeneous semiconductor. If these conditions are not fulfilled, then the electronic component of Eq. (39) must be used to quantify PCR contrast due to distributed subsurface electronic defect structures.

The mild mechanical defect on the back surface of the p-type Si wafer that generated the images of Figs. 10 and 11 proved to be too severe for our sensitive InGaAs photodetector: upon scanning the affected surface, the PCR signal vanished within the region of the defect, apparently due to the highly efficient trapping of the photogenerated free carriers by the high density of near-surface electronic defect states. Therefore, a different region of the same wafer was chosen to create a visually undetectable defect by simply touching the back surface of the wafer with paper. Then both the PTR and PCR frequency scans were performed on both sides of the material, outside and inside the defect region. Figure 13 shows the PTR amplitudes and phases for all four spots, as

well as theoretical fits to the experimental data. The curves were normalized for the instrumental transfer function, including the MCT detector and preamplifier, by a zirconia reference sample of known thermophysical properties. The PTR theoretical model was a superposition of carrier wave and IR emissions of thermoelectronic origin using coupled field expressions (Ref. 14, Chap. 9.12), with adjustable thermal and electronic coefficients, C_t and C_p, respectively.[4,5] The effect of the back-surface defect was modeled as a change in S_2 (front-surface probing) only. When the wafer was turned over, the definitions of S_1 and S_2 were reversed. It will be noted that the results of the theoretical fits to data obtained from the front (polished) surface of the wafer clearly indicate an increase in S_2 inside the region with the back-surface defect. At the same time, the ambipolar diffusion coefficient D^* increased from 12 cm^2/s to 15 cm^2/s. This is probably due to the steepening of the CW spatial gradient across the bulk of the wafer as a result of depletion at the back surface, which tends to increase the carrier-diffusion-wave flux toward the bulk of the sample and thus increase the effective value of D^*. The absolute value range of D^* is within the accepted values of hole diffusivity in *p*-type Si.[5] Upon turning the sample over, the τ and D^* values did not change much from those measured from the polished side, however, the absolute values of S_1 (formerly S_2) and S_2 (formerly S_1) changed significantly, with the damaged surface value increasing from 450 cm/s to 650 cm/s. The other surface recombination velocity values also show changes. The reason for these discrepancies probably lies with the values being spatial averages over nonuniform subsurface regions of the sample bulk sampled under the PTR probe, as spreading spherical CW diffusion below the surface of the wafer probably encounters electronically and thermally inhomogeneous regions, especially in the neighborhood of the affected spot. The differences in texture of the polished and matte surfaces as seen by diffusing carrier waves from the inside of the material may also be a factor affecting the mean surface recombination velocities. Figure 14 shows the PCR frequency scans at exactly the same spots as Fig. 13. Here, signal normalization was performed by extracting the CW component of the PTR signal, i.e., the depth integral over $\Delta N(r,z,\omega)$, Eq. (49), associated with the prefactor C_p in the front intact region of Fig. 13, and making it the reference PCR signal for the same region. The thus obtained PCR amplitude and phase transfer functions were subsequently used for all other measurements. The theoretical phase fits to the PCR data show better agreement at the highest frequencies than the respective PTR fits, a feature observed with other Si experiments as well. The τ values are similar to their PTR counterparts. Regarding the D^* values those outside the defect remain constant for both sides of the wafer, however, the D^* value from the back inside the defect region is relatively low. The higher sensitivity of the InGaAs detector to the electronic state of the inspected surface is probably responsible for this discrepancy, as the theoretical phase fit is poor at high frequencies (>1 kHz) within that region, an indication of near-surface depth inhomogeneity of transport properties. On the other hand, the PTR phase is less sensitive to the electronic component, resulting in a much better (and very likely artificial) fit, Fig. 13(b). Regarding the surface recombination velocities, similar trends to the PTR results are observed, with the PCR showing different (lower) absolute values within the damaged region. This is a consistent trend also observed with other damaged Si wafers, for which PTR usually yields higher (or much higher) values. It can be explained by the strong nonradiative energy conversion character of poor surfaces and the PTR ability to monitor thermal-infrared emissions superposed on purely recombination IR emissions. This superposition tends to amplify the effect of enhanced nonradiative recombination on poor surface conditions and to yield increased effective values of the respective velocities. In summary, comparison of Figs. 13 and 14 and the resultant theoretical fits show that the PCR signals are very sensitive to the electronic state of the probed semiconductor surface and bulk, whereas the PTR signals can be subtly or grossly masked by thermal-wave contributions which may significantly affect the values of the photoexcited carrier transport properties. It is also shown that the theoretical/computational extraction of the electronic component from the PTR signal superposition[4,5] may not be entirely accurate or complete.

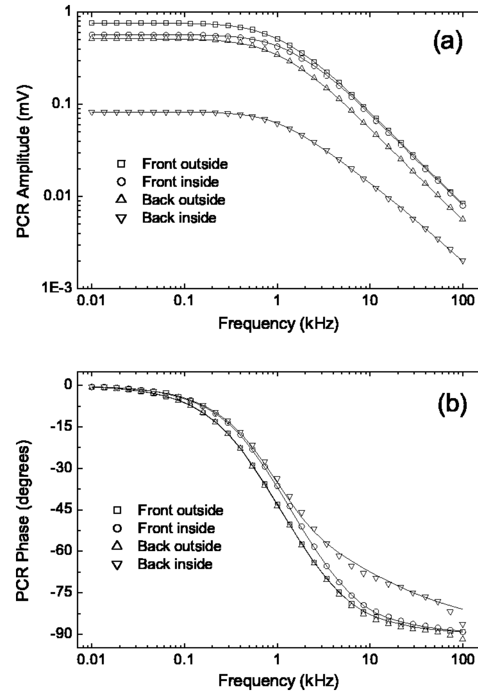

FIG. 14. Front- and back-surface PCR frequency scans inside and outside a defect area of a *p*-Si wafer on aluminum backing. Detector, InGaAs; beam size, 1.4 mm; Ar-ion laser power, 20 mW. (a) Amplitudes and (b) phases. Best fit parameters. Front intact region: $\tau=1$ ms, $D^*=12$ cm^2/s; $5S_1=10$ cm/s; $S_2=210$ cm/s. Front inside the defect: $\tau=1$ ms, $D^*=14.9$ cm^2/s; $S_1=25$ cm/s; $S_2=300$ cm/s. Back intact region: $\tau=1$ ms, $D^*=12$ cm^2/s; $S_1=10$ cm/s; $S_2=200$ cm/s. Back inside the defect: $\tau=1$ ms, $D^*=5$ cm^2/s; $S_1=450$ cm/s; $S_2=130$ cm/s.

V. CONCLUSIONS

Photocarrier Radiometry (PCR) has been introduced as a high contrast, sensitive, and quantitative electronic materials

inspection technique and several comparisons with the conventional PTR of semiconductors have been performed. The technique depends on an optimized infrared photon detection circuit, with the infrared detector spectral window being matched to the recombination emission spectrum of the semiconductor under investigation. As such, PCR filters out entirely the thermal-infrared component of the spectrum and thus monitors purely electronic phenomena. First reported applications include scanning imaging of deep subsurface electronic defects and quantitative measurements of the major transport properties of Si wafers: carrier recombination lifetime, ambipolar diffusion coefficient, and surface recombination velocities. A noteworthy feature of the high-frequency PCR imaging is the so far unappreciated very long-range effect of carrier interactions with deep subsurface defect structures and the detrimental ability of such structures to decrease the overall free photoexcited-carrier density in locations far away from the defect sites at or near the front surface where device fabrication takes place. Therefore, PCR may become an important tool toward device fabrication improvement through careful selection of substrate wafers with regard to deep bulk growth and manufacturing defects that were heretofore not associated with device performance.

ACKNOWLEDGMENTS

The continuing support of the Natural Sciences and Engineering Research Council of Canada (NSERC) is gratefully acknowledged. J.B. also acknowledges CNPq (Conselho Nacional de Desenvolvimento Cientifico e Tecnologico—Brazil) for its support.

*On leave from Departamento de Fisica, Universidade Federal do Maranhao, Sao Luis, MA, Brazil. Electronic address: jbatista@ufma.br

[1] A. Mandelis, R. Bleiss, and F. Shimura, J. Appl. Phys. **74**, 3431 (1993).
[2] A. Mandelis, A. Othonos, C. Christofides, and J. Boussey-Said, J. Appl. Phys. **80**, 5332 (1996).
[3] A. Othonos, C. Christofides, and A. Mandelis, Appl. Phys. Lett. **69**, 821 (1996).
[4] T. Ikari, A. Salnick, and A. Mandelis, J. Appl. Phys. **85**, 7392 (1999).
[5] M.E. Rodriguez, A. Mandelis, G. Pan, L. Nicolaides, J.A. Garcia, and Y. Riopel, J. Electrochem. Soc. **147**, 687 (2000).
[6] A. Mandelis and Y. Riopel, J. Vac. Sci. Technol. A **18**, 705 (2000).
[7] M.E. Rodriguez, A. Mandelis, G. Pan, J.A. Garcia, V. Gorodokin, and Y. Raskin, J. Appl. Phys. **87**, 8113 (2000).
[8] A. Mandelis, M.E. Rodriguez, Y. Raskin, and V. Gorodokin, Phys. Status Solidi A **185**, 471 (2001).
[9] M.E. Rodriguez, A. Mandelis, G. Pan, J.A. Garcia, and Y. Riopel, Solid-State Electron. **44**, 703 (2000).
[10] N. Mikoshiba and K. Tsubouchi, in *Photoacoustic and Thermal-Wave Phenomena in Semiconductors*, edited by A. Mandelis, (North-Holland, New York, 1987), Chap. 3; C. Christofides, A. Othonos, and K. Kalli, Electrochem. Soc. Proc. **29**, 153 (2001).
[11] A. Mandelis, R.A. Budiman, M. Vargas, and D. Wolff, Appl. Phys. Lett. **67**, 1582 (1995).
[12] A. Mandelis, Solid-State Electron. **42**, 1 (1998).
[13] C. Christofides, M. Nestoros, and A. Othonos, in *Semiconductors and Electronic Materials*, edited by A. Mandelis and P. Hess, Progress in Photoacoustic and Photothermal Phenomena Vol. IV (SPIE, Bellingham, WA, 2000), Chap. 4.
[14] A. Mandelis, *Diffusion-Wave Fields: Mathematical Methods and Green Functions* (Springer-Verlag, New York, 2001), Chap. 9.
[15] R.E. Wagner and A. Mandelis, Semicond. Sci. Technol. **11**, 300 (1996).
[16] A. Salnick, A. Mandelis, H. Ruda, and C. Jean, J. Appl. Phys. **82**, 1853 (1997).
[17] S.J. Sheard, M.G. Somekh, and T.M. Hiller, Mater. Sci. Eng., B **5**, 101 (1990).
[18] A. Rosencwaig, in *Photoacoustic and Thermal-Wave Phenomena in Semiconductors*, edited by A. Mandelis (North-Holland, New York, 1987), Chap. 5.
[19] A. Mandelis, A. Salnick, L. Chen, J. Opsal, and A. Rosencwaig, J. Appl. Phys. **85**, 1811 (1999).
[20] R.E. Wagner and A. Mandelis, Semicond. Sci. Technol. **11**, 289 (1996).
[21] A. Mandelis and R.E. Wagner, Jpn. J. Appl. Phys., Part 1 **35**, 1786 (1996).
[22] R.N. Hall, Inst. Electr. Eng. 106B, Suppl. **17**, 923 (1959).
[23] W. van Roosbroeck and W. Shockley, Phys. Rev. **94**, 1558 (1954).
[24] G. Kirchhoff, *Abhandlungen über Emission und Absorption,* edited by M. Planck (Verlag von Wilhelm Engelmann, Leipsig, 1898), pp. 11–36.
[25] J.S. Blakemore, *Semiconductor Statistics* (Dover, New York, 1987), Chap. 4.
[26] M.A. Weinstein, Am. J. Phys. **28**, 123 (1960).
[27] A. Bauer, Optik (Stuttgart) **29**, 179 (1969).
[28] G. Chen, T. Borca-Tasciuc, and R.B. Fair, J. Appl. Phys. **82**, 830 (1997).
[29] R. Siegel and J.R. Howell, *Thermal Radiation Heat Transfer* (Hemisphere, Washington, 1992).
[30] P.J. Timans, J. Appl. Phys. **74**, 6353 (1993).
[31] F.A. Johnson, Proc. Phys. Soc. London **73**, 265 (1959).
[32] D.K. Schroder, R.N. Thomas, and J.C. Swartz, IEEE Trans. Electron Devices **25**, 254 (1978).
[33] R.A. Smith, *Semiconductors*, 2nd ed. (Cambridge University Press, Cambridge, 1978), pp. 118–119.
[34] S.J. Sheard and M.G. Somekh, Electron. Lett. **23**, 1134 (1987).
[35] F. Kreit and W.Z. Black, *Basic Heat Transfer* (Harper & Row, New York, 1980).
[36] Judson Technologies Detector Offerings; www.judtech.com
[37] A. Mandelis (unpublished).
[38] R.D. Tom, E.P. O'Hara, and D. Benin, J. Appl. Phys. **53**, 5392 (1982).
[39] M.E. Rodriguez, J.A. Garcia, A. Mandelis, C. Jean, and Y. Riopel, Appl. Phys. Lett. **74**, 2429 (1999).